Cobalt-Doped Manganese Dioxide Hierarchical Nanostructures for Enhancing Pseudocapacitive Properties

Sarika M. Jadhav, Ramchandra S. Kalubarme, Norihiro Suzuki, Chiaki Terashima, Junyoung Mun, Bharat Bhanudas Kale, Suresh W. Gosavi,* and Akira Fujishima
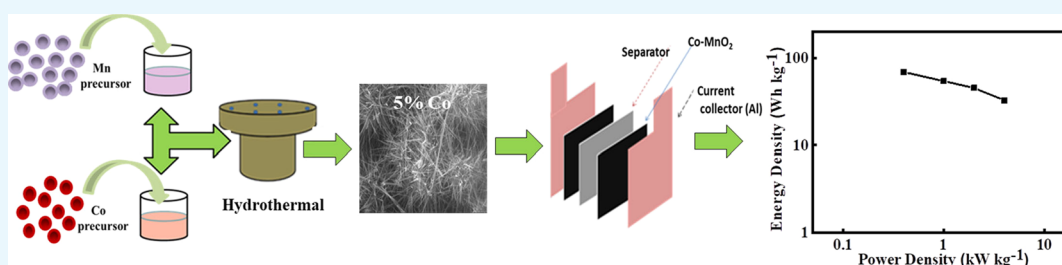
Read Online

ACCESS | Metrics & More | Article Recommendations | Supporting Information

ABSTRACT: Herein, overall improvement in the electrochemical performance of manganese dioxide is achieved through fine-tuning the microstructure of partially Co-doped manganese dioxide nanomaterial using facile hydrothermal method with precise control of preparative parameters. The structural investigation exhibits formation of a multiphase compound accompanied by controlled reflections of α-MnO$_2$ as well as γ-MnO$_2$ crystalline phases. The morphological examination manifests the presence of MnO$_2$ nanowires having a width of 70−80 nm and a length of several microns. The Co-doped manganese dioxide electrode displayed a particular capacitive behavior along with a rising order of capacitance concerning with increased cobalt ion concentration suitable for certain limits. The value of specific capacitance achieved by a 5% Co-doped manganese dioxide sample was 1050 F g^{-1} at 0.5 A g^{-1}, which was nearly threefold greater than that achieved by a bare manganese dioxide electrode. Furthermore, Co-doped manganese dioxide nanocomposite electrode exhibits exceptional capacitance retention (92.7%) till 10,000 cycles. It shows the good cyclability as well as stability of the material. Furthermore, we have demonstrated the solid-state supercapacitor with good energy and power density.

1. INTRODUCTION

During the recent decade, the transformation of nonrenewable sources toward renewable energy sources has been given ample prominence owing to limited fossil fuel supply and worldwide environmental conservation. Because of the recurrent nature of renewable sources such as (wind and solar, etc.) extra renewable manufacture is required to store for later utilization. Storage of energy plays a crucial role in minimizing or avoiding the prices demanded throughout the peak time interval by a specific entity. In that situation, electrochemical capacitors known as supercapacitors and batteries are the ideal contenders for the upcoming energy dilemma. Storage of electrochemical energy through rechargeable batteries is important for growth. Aqueous rechargeable cells are the reasonable and secure alternative for power storage after renewable generation. Substantial analysis and investigation are going on to establish an eco-friendly, earth-abundant, cost-effective, and new energy storage material having high specific capacity and energy density along with enhanced cyclability. Among different emerging energy storage technologies, the supercapacitor is the most promising technology because of its long cycle life, outstanding charge and discharge, and the

potential to transfer more power than usual batteries, and also, favorable energy storage devices have high energy density for hybrid electric vehicles.[1,2] Supercapacitors have been attracting substantial recognition as a performance bridge gap between the high power density of an electrolytic capacitor and the high energy density of a battery.[3] Based on the energy storage mechanism, they can be classified into two different sets, namely, electric double-layer capacitors (EDLCs) and pseudocapacitors. In EDLCs, the stemming of charges is from electrostatic accumulation at the interface of an electrolyte/electrode in an electric double layer. For EDLCs, carbon-based materials having a huge surface area, for example, porous activated carbon,[4] activated carbon fiber cloths/fabrics,[5] carbon nanotubes,[6] graphene,[7] and carbon aerogels[8] are targeted as electrode materials. In pseudocapacitors, energy

is stored through surface faradic redox reactions of electroactive materials, which exhibit higher theoretical capacitance than EDLCs.[9] Electroactive materials such as transition metal oxide/hydroxide,[10] sulfides,[11] and conductive polymers[12] have several oxidation states, which are responsible for effective redox charge transfer,[13] and so they exhibit considerable responsiveness in energy storage applications. Owing to the high energy density and specific capacitances of the above-mentioned materials, they can fulfill the requirement of high energy density and high power density in modern devices better than carbon-based EDLCs. With an ever more intensifying requirement of rechargeable batteries, transition metal oxide-based electrochemical capacitors like MnO_2,[14] RuO_2,[15] Co_3O_4,[16] NiO,[17] V_2O_5,[18] Fe_2O_3,[19] and CuO[20] have received more recognition in the market as electrode materials because of their distinct electrochemical properties. It is reported that RuO_2 has eminent electrochemical properties and a high value of specific capacitance [1340 F/g at a 25 mV scan rate by cyclic voltammetry(CV)], but its toxicity and high price affect its application propects.[9] Among all transition metal oxides, manganese dioxide (MnO_2) is the best alternative to RuO_2, which is one of the best electrode materials for pseudocapacitors owing to its adequate energy storage performance in mild aqueous electrolytes, earth abundance, environmental friendliness, low cost, low toxicity,[21,22] and high value of theoretical specific capacitance (1370 F/g).[23] The MnO_2 electrode has a pseudocapacitive charge storage mechanism, which means that a fast faradaic redox reaction occurs on the inner side of the bulk materials or near the surface of the electrode across the significant range of potentials.[24] To exhibit an excellent capacitive performance, there is a need for the electrode material to have a large surface area and fast transfer of ions/electrons. However, low surface areas and deficient electrical conductivity ($10^{-5} - 10^{-6}$ S cm^{-1}) of MnO_2 restrict the rate of charging and discharging for high-performance supercapacitors.[25,26] This inspires wide interest to take efforts to integrate MnO_2 nanostructures with conducting polymers or carbon-based materials.[27,28] By combining eccentric properties of the separate components, cycling ability and enhancement in rate capability could be accomplished in such carbon-based metal oxide electrodes. Rather than this, another problem of MnO_2-based materials emerges because of the loading of less active material, which leads to a lower energy density. Hence, magnifying the electrochemical usage of the pseudocapacitance of MnO_2 by reasonably scheming MnO_2-based electrodes with innovative structures and dependable electric interconnection is still a big problem. Another magnificent material for the supercapacitor electrode is cobalt oxide, and incorporation of Co ions in MnO_2 leads to better pseudocapacitive performance.[29] Co-doped MnO_2 nanocomposites show significant enhancement in electrode conductivity, and published research work based on Co-MnO_2 also indicates that it can be an encouraging electrode material for supercapacitor applications.[30] Specific capacitance depends not only on conductivity and transport properties but also on the surface area of the electrode material. Different morphological architectures of MnO_2 including nanoflakes, nanorods, nanoflowers, nanowires, and nanosheets[31−35] had been synthesized and efficiently analyzed for the study of electrochemical performance. There are different techniques and methods available for the synthesis of the nanomaterials that have several morphologies, but mainly, a simple hydrothermal method was approved for synthesizing the different morphological MnO_2 nanostructures that are mentioned in experimental section 4. Generally, the hydrothermal method is a simplified and effective green synthesis method for developing nanomaterials of various shapes and sizes; by modifying the pH, time, temperature, and solvent used in the chemical reaction. By using this simple hydrothermal method, nanostructured materials having a huge reactive surface area can be efficiently produced on a massive scale.[36]

Herein, favorable synthesis of Co-doped MnO_2 tiny nanowires was demonstrated in one step by using a simple hydrothermal method for high-performance electrochemical supercapacitors. Various molar percentages of Co (1, 2, 4, 5, and 10%) were incorporated in MnO_2, which plays an important role in greatly enhancing their electrochemical properties. Therefore, the electrochemical performance of manganese dioxide nanocomposite electrode exhibits increase in its specific capacitance value of 1050 F g^{-1} at the applied current density of 0.5 A g^{-1}. Furthermore, a prototype solid-state supercapacitor developed using a prepared electrode demonstrated superior performance regarding long cycle life and superior capacity retention along with improved flexibility, mechanical strength, and reduced weight.

2. RESULTS AND DISCUSSION

The pristine manganese oxide (S_0) and manganese oxide with Co doping percentage of 1% (S_1), 2% (S_2), 4% (S_3), 5% (S_4), and 10% (S_5) were prepared by a one-step hydrothermal process.

2.1. X-ray Diffraction Analysis. The X-ray diffraction (XRD) pattern is studied for structural analysis of all the obtained powder samples (S_0−S_5), which is shown in Figure 1(a−f). All the synthesized nanocomposite samples exhibit a similar trend of diffraction pattern having several crystalline phases dominating the α-MnO_2 tetragonal phase (JCPDS 44−0141). Furthermore, the additional diffraction peaks are related to the γ-type MnO_2 phase (JCPDS-14-0644). In the present case, the mixed phases of the MnO_2 nanocomposite were synthesized at similar reaction conditions, as explained in the experimental section.

Because of the addition of Co precursor, under the changed hydrothermal condition (pH of the reaction solution and the cation availability), partial transformation of a 2 × 2 tunnel structure (α-MnO_2) into a 1 × 2 (γ-MnO_2) structure might occur. Moreover, a time relaying hydrothermal reaction can simply impact the crystallization of MnO_2 or convert it to different phases, as mentioned in the literature.[37] After Co addition, the peaks of the typical phase related to metallic Co or its oxide were not observed. Furthermore, there is a slight shift in the peak position to lower 2θ degrees, which implies the Co species doped in a highly dispersed state.[38] The crystalline size of the Co-doped MnO_2 samples is calculated by the Debye−Scherrer formula, which ranges between 20 and 50 nm for different mol %. From the XRD pattern, we observed that with increasing cobalt content, there is a decrease in crystalline size, and also, no extra peaks corresponding to the cobalt oxide phase were seen in the Co-doped MnO_2. However, few MnO_2 peaks at 37 and 43^0 have been merged with cobalt oxide. Hence, detailed investigation is performed using Raman analysis.

2.2. Raman Spectroscopy. Raman spectra of synthesized materials enable us to identify the explicit changes in scattering
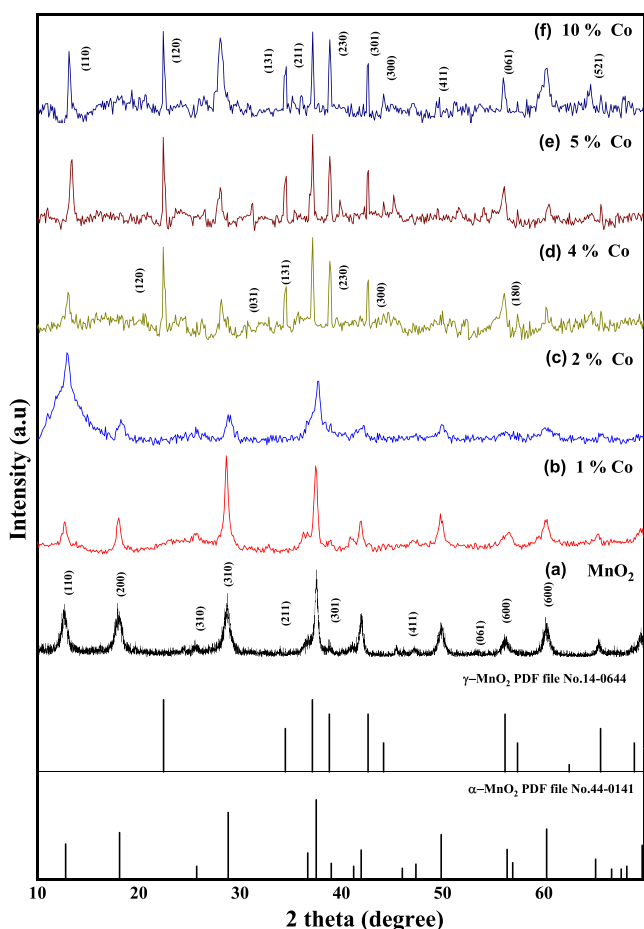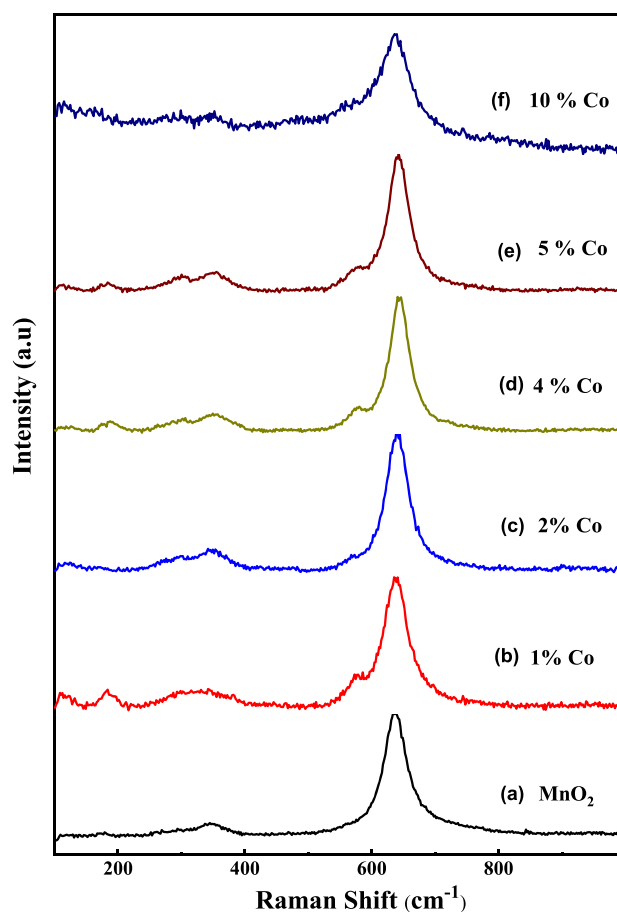
Figure 1. XRD pattern of (a) pristine MnO_2 and (b) 1%, (c) 2%, (d) 4%, (e) 5%, and (f) 10% Co-doped MnO_2.

Figure 2. Raman spectra of (a) pristine MnO_2 and (b) 1%, (c) 2%, (d) 4%, (e) 5%, and (f) 10% Co-doped MnO_2.

due to doping of cobalt in the MnO_2 nanocomposite, as shown in Figure 2.

In Raman spectra of bare MnO_2 (S_0) (Figure 2a), three peaks are observed at 180, 344, and 636 cm^{-1}, which correspond to the O-Mn-O stretching vibration, Mn-O stretching vibration in the basal plane of the MnO_6 group, and Mn-O symmetric stretching vibration of the MnO_6 group, which has double the chains of MnO_2, respectively.[31] In Figure 2(b-f), two major peaks are noticed at 572 and 640 cm^{-1}, which have the characteristics of the synthesized material. Specifically, in Raman spectra of various Co mol % samples, a weak peak present at 572 cm^{-1} corresponds to the Mn−O lattice vibration in MnO_2.[39] All three characteristic peaks that are mentioned above are observed in each Raman spectrum of the Co-doped MnO_2 nanocomposite. Remarkably, because of the incorporation of Co, higher frequency shift is observed. For the lower doping concentration (1% Co) of the sample (S_1), the characteristic peak shift is observed at 182, 348, and 638 cm^{-1}. In the case of 2, 4, 5, and 10% Co-doped MnO_2 (S_2–S_5) samples, the shift in the peak further deteriorates. The peak present at 636 cm^{-1} shifted to 640 cm^{-1}, which suggests the strengthening of the (Mn, Co)−O bond. It also shows that incorporation of Co into the lattice ensures the change in the structural lattice parameter.

2.3. Morphological Analysis. Scanning electron microscopy (SEM) analysis examined the topographical composition of the synthesized Co-doped manganese dioxide nanosystem. Figure 3 (a) shows the bare MnO_2 (S_0) sample, where we

observed α-MnO_2 nanowires having micrometer length and tens of nanometers width along with a high aspect ratio. It also shows wrinkles and a scratchy texture, which play a key role in the charge storage mechanism. Figure 3(b-f) reveals the SEM images of S_1–S_5 samples, respectively. By observing SEM images, it can be seen that all the synthesized nanocomposite samples show the morphology of agglomerated Co-doped MnO_2 tiny nanowires with their length in the 1 to 5 μm range and diameter of few nanometers. From Figure 3(f), we observed that the morphology of agglomerated microspheres has a diameter in the 1−3 μm range for S_5. As the concentration of doping increases, the particles get agglomerated and exhibit more enhanced edge connection of grains. Because of the stronger diffusion of dopant ions in manganese oxide, the particles are more densely packed and are compact; therefore, in the S_5 sample, microsphere clusters are observed.[40,41] From SEM images, we can conclude that at a high concentration of cobalt, the one-dimensional growth of MnO_2 has been suppressed drastically, which affects the morphology of the nanocomposite.

The elemental study of manganese dioxide nanocomposites is carried out with EDS as shown in Figure 3(g), which confirm the existence of Mn and O in the synthesized nanomaterial. Further peaks are seen at 1.2, 2.2, and 2.4 keV, which are coated in platinum for the purpose of preventing charging of the nanomaterial at the time of imaging. The EDS study of doped manganese dioxide nanocomposites, which are exhibited in Figure 3(h), provides elemental confirmation and
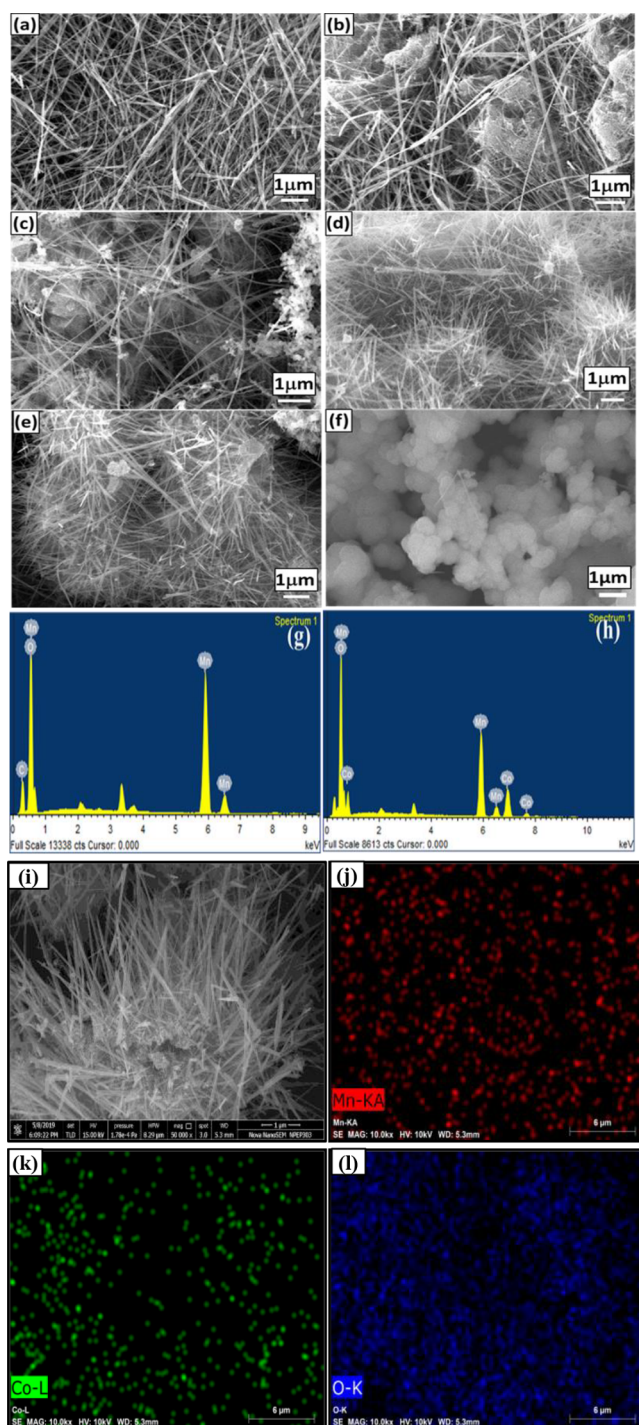
Figure 3. SEM images of (a) pristine MnO_2 (S_0) and (b) 1% (S_1), (c) 2% (S_2), (d) 4% (S_3), (e) 5% (S_4), and (f) 10% Co-doped MnO_2 (S_5) powder samples. EDS spectra of (g) S_0 and (h) S_4. EDS mapping of S_4 (i-l).

indicates integration of Co ions present in the composite; the sample contains Mn, O, and Co only. Additionally, the peak present at 3.4 keV indicated the existence of potassium in both the nanocomposites, which are essential for stabilizing the 2 × 2 (α-MnO_2) and 2 × 1 (γ-MnO_2) tunnel structures. EDS mapping of the S_4 sample is shown in Figure 3(i-l). It can be observed that the selected area of the S_4 sample confirms the existence of manganese [Figure 3(j), red], cobalt [Figure 3(k), green], and oxygen [Figure 3(l), blue] elements on the entire

surface of material. From EDS mapping of the S_4 sample, atomic percentage at different spots or selected areas was also determined and is given in Table S1. The average percentages of manganese, oxygen, and cobalt present in the sample are 21.63, 73.53, and 4.83%, respectively with uniform distribution on the sample, and the values are in good agreement with the designed compositions.

The transmission electron microscopy (TEM) images in Figure 4(a) show the Co-doped manganese dioxide nano-
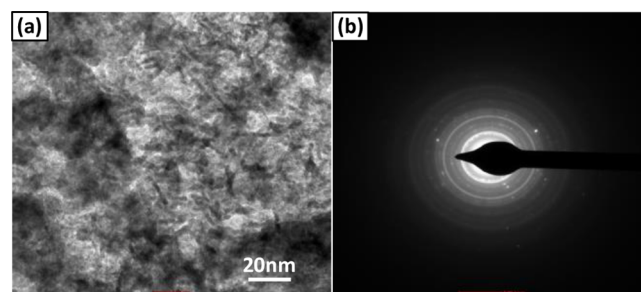
**Figure 4.** TEM images of the S4 sample. (a) High-resolution TEM image and (b) SAED pattern.

composite composed of ultrathin nanowires, as evidence with SEM images and the selected area electron diffraction (SAED) pattern in Figure 4(b) show the polycrystalline nature of the synthesized nanocomposite.

2.4. X-ray Photoelectron Spectroscopy Analysis. To clarify the elemental composition of the Co-doped MnO_2 sample, X-ray photoelectron spectroscopy (XPS) was performed, which is shown in Figure 5. The wide survey spectrum of the Co-doped MnO_2 sample [Figure 5(a)] shows the presence of cobalt, manganese, and oxygen. The Co2p high-resolution deconvoluted spectrum [Figure 5(b)] shows a peak at 780.5 and 795.5 eV relative to Co $2p^{3/2}$ and Co $2p^{1/2}$ peaks of cobalt. These two peaks are further divided into four more fitting peaks, which show the presence[42,43] of Co^{2+} and $Co.^{3+}$ The peak difference between spin-orbit doublets is 15.0 eV, which suggests the interaction of two energy levels. The satellite peaks present at 786.1 and 805.2 eV confirm the presence of Co^{2+} and Co^{3+} in the Co-doped MnO_2 sample. Similarly, the high-resolution deconvolution spectrum of Mn2p [Figure 5(c)] exhibits the peak at binding energies 642.2 and 653.6 eV, which are related to $2p^{3/2}$ and $2p^{1/2}$ peaks of Mn^{3+}, and these spin orbits are separated from each other by spin energy 11.4 eV, which is the same as has been already reported for manganese-based materials.[44] In contrast, the peaks present at 644.2 and 654.7 eV are assigned to $2p^{3/2}$ and $2p^{1/2}$ of Mn^{4+} ions. It indicates the redox couple species of Co^{2+}/Co^{3+} and Mn^{3+} and Mn^{4+} present in Co-doped MnO_2 nanocomposites.[45] Moreover, the O1s high-resolution spectrum shown in Figure 5(d) consists of a peak at 531.5 and 533.3 eV, which correspond to oxygen atoms in the hydroxyl group and absorbed water and a dominant peak at 529.9 eV, which is related to oxygen atoms in oxides of MnO_2.[46] From survey XPS, the calculated contents of manganese and oxygen are 22.99 and 52.19%, respectively. The cobalt-doping concentration observed by the XPS survey result is 4.37%, which is approximately equal to the experimentally designed concentration for doping in MnO_2. In a nutshell, the XRD, EDS, Raman, and XPS results show the presence of cobalt oxide along with all MnO_2 phases.
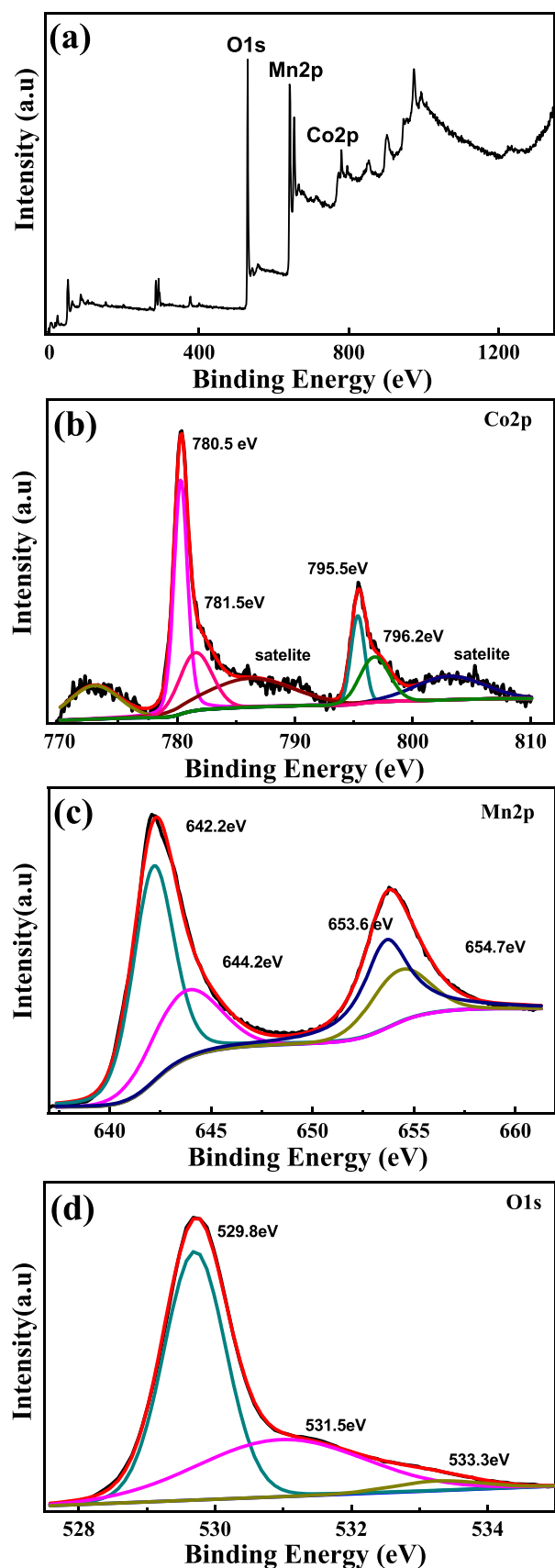
Figure 5. Wide scan spectra of 5% Co-doped MnO_2 (a) and XPS spectra of Co2p (b), Mn2p (c), and O1s (d).

Nitrogen adsorption−desorption experiments were performed at 77 K to analyze the porous structure of the as-prepared Co-doped MnO_2 nanocomposite. Figure 6(a) shows
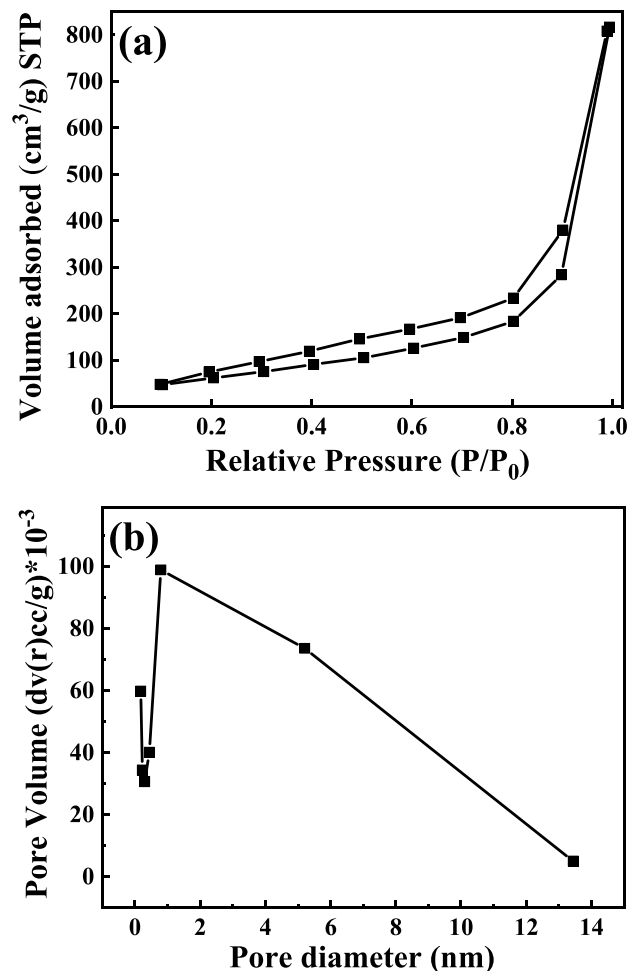

Figure 6. (a) Nitrogen adsorption−desorption curve and (b) BJH pore size distribution curve of the Co-doped MnO_2 nanocomposite.

the H3 hysteresis loop over a relative pressure range of 0.1 < P/P_0 < 0.9, which indicated a specific type IV isotherm. These results are in agreement with the presence of microporous materials, as claimed by the IUPAC classification.[47] They are archetypally cage-like pore structures having a large number of mesopores and slender channel connections. In another way, the nonlocal density functional theory algorithm technique was applied to examine the pore size distribution curve of the Co-doped MnO_2 nanocomposite. It can be seen in Figure 6(b) that pore size distribution of broad micropores and mesopores is done by the desorption branch in the range of 1−8 nm.

Hence, the Co-doped MnO_2 nanocomposite was incorporated into the doubly porous structure of micropores and mesopores. That range of pore size can deliver better electrolyte penetration and access during the charging−discharging test. Moreover, it was anticipated that a steady surrounding lead to insertion/extraction of hydroxyl ions in the charge/discharge cycling, where the boosted cycle life is noticed for the assembled electrode.[48] Furthermore, the surface area of Co-doped MnO_2 nanocomposites observed from Brunauer−Emmett−Teller analysis was around 249.7 m^2/g, and that high surface area provides more adsorption

sites. Therefore, it suggests that the synthesized material exhibits excessive supercapacitive performance.

2.5. Electrochemical Performance. To analyze the electrochemical performance of MnO_2 and Co-doped MnO_2 electrodes, CV was performed in the 1 M Na_2SO_4 electrolyte solution in the range of 0−0.8 V at a scan rate of 50 mVs^{-1}, which is shown in Figure 7.
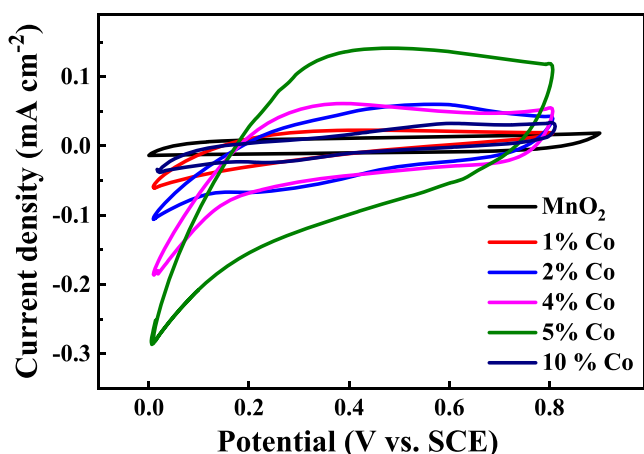
Figure 7. CV curve of S_0, S_1, S_2, S_3, S_4, and S_5 electrodes in the 1 M Na_2SO_4 electrolyte at a 50 mVs^{-1} scan rate.

By observing the CV curves, it can be seen that all the samples exhibit typical rectangular shapes like MnO_2 pseudocapacitors; this is hardly affected by the presence of Co^{2+} cations. The surface faradaic reaction of prepared sample electrodes reveals that adsorption of Na^+ cations and H_3O^+ protons on the surface having rapid reversible consecutive surface redox reactions of the synthesized nanocomposite electrode by the intercalation/deintercalation process takes place according to the eq 1.[49,50]

$$MnO_2 + Na^+ + e^- \; (MnOONa)_{surface} \qquad (1)$$

However, no distinctive redox peaks were noticed in the CV curve of the prepared electrodes, which shows charging and discharging of the electrode at a pseudoconstant rate of the entire voltammetric cycle having a pseudocapacitive nature. Specific capacitance (C F g^{-1}) of CV curves is calculated by using the following formula 2.[51]

$$C = \frac{1}{2m\upsilon(V_b - V_a)} \int_a^b Idv \qquad (2)$$

where m(gm) is the loaded mass of the active material on the working electrode, υ (V s^{-1}) is the potential scan rate, I (A) is the voltammetric current or discharge current, and V_b and Va(V) are high and low potential limits used to record the CV curve.

The volumetric charges in all Co-doped electrodes are higher than those in pure MnO_2 oxide, which shows that Co doping enhanced specific capacitance and electrical conductivity because of the introduction of Co in the Mn oxide framework. In the potential region examined, transition of Mn^{4+}/Mn^{3+} involving single-electron transfer is responsible for the pseudocapacitive behavior of the Co-doped Mn oxide. The calculated values of capacitance for S_0, S_1, S_2, S_3, S_4, and S_5 electrodes at a sweep rate of 50 mVs^{-1} were 102, 341, 376,

468, 983, and 132 Fg^{-1}, respectively. The achieved value of specific capacitance and enhancement in the related current of the CV curve confirmed the impact of Co ions on the electrochemical behavior of MnO_2 nanocomposite. The 5% Co-doped MnO_2 (S_4) sample shows a high capacitance value, which is ninefold greater than bare MnO_2 (S_0) electrode. This may be due to the presence of another more remarkably electrochemically active system of α-MnO_2 and γ-MnO_2 in the synthesized nanomaterial. Even if these nanomaterials have less surface area, they can show maximum specific capacitances because of the appropriate form of their tunnel structure along with the proper hydrate content that encourages the Faradaic behavior.[52,53] The specific capacitance value for 10% Co-MnO_2 (S_5) was seen to be decreasing in comparison with other Co-doped synthesized samples that exhibit a positive impact on Co ion doping extended to particular limits in the MnO_2 nanocomposite. It may be due to agglomeration of particle, making the nanocomposite bulky and thus prohibiting the reaction of core MnO_2 and the electrolyte. The shielding effect due to cobalt is also due to the morphology, where a cluster of particles hinder the electron transfer at the surface. The 5% Co-MnO_2 (S_4) sample exhibits highly crystalline nanowires deposited with cobalt oxide tiny nanoparticles, which enhance the overall conductivity via increasing the transport of electrons at the surface. Hence, the higher capacitance obtained for this sample is quite understood.

Figure 8 shows the graph of change in peak current density versus the square root of the scan rate. The linear relationship
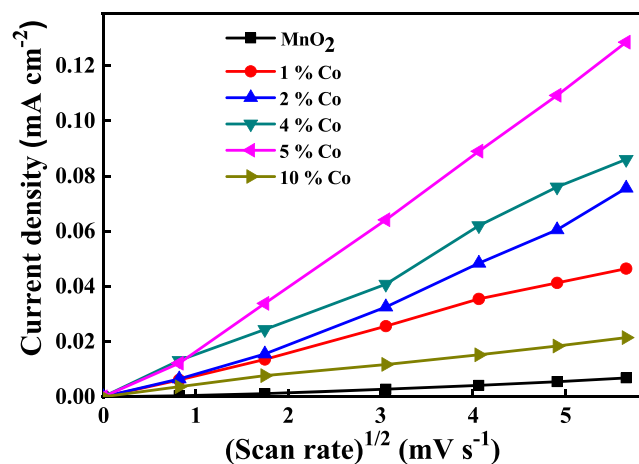
Figure 8. Current density vs square root of the scan rate for the Co-doped MnO_2 composite electrode in the 1 M Na_2SO_4 electrolyte.

between current density and scan rate indicates surface redox reaction, and diffusion-controlled reaction occurs during the electrochemical process.[54]

Co-doped MnO_2 nanocomposite materials can boost the rate of electron transfer because of their quite high conductivity and large surface area; hence, the redox reaction that occurs at the interface of the electrode is diffusion-controlled instead of the kinetic one. The variation in the specific capacitance value of bare MnO_2 and Co-doped MnO_2 with different scan rates in the 1 M Na_2SO_4 electrolyte is exhibited in Figure S1. It can be noticed that as the scan rate increases, the specific capacitance value decreases. At the sweep rate of 10 mVs^{-1}, bare MnO_2 has a specific capacitance of approximately 110 F g^{-1}, and after doping of cobalt in MnO_2, the value of specific capacitance increased approx-

imately to 1500 F g^{-1}. Generally, the redox reaction depends on the rate of insertion/extraction of protons or cations in the electrolytes.[55] At the slow scan rate, high specific capacitance was observed because of the slow charging–discharging process, wherein solvated ions/cations slowly diffused into the electrode and accessed almost all the available pores or active sides until all active sides were fully adsorbed and the material was wholly utilized. At the fast scan rate, protons/cations did not get enough time to adsorb on whole active sides of material, and so they could not be fully utilized, which resulted in low specific capacitance.[56] Hence, a good characteristic property of the synthesized Co-doped MnO$_2$ capacitive nanomaterial was observed also at low sweep rate because of embracing working protons/cations at the active site, which leads to efficient interaction among the cations and electrodes.

The total charge stored in the material during the faradic and nonfaradic reaction is represented by the area under the CV curve. In the faradic process, charge originated from redox reaction, whereas for the nonfaradic process, it arises from double layer formation. By examining the CV curves at various sweep rates (υ), the effect of these processes can be studied with the help of the power law.[57] According to the power law, $I = a\,\upsilon^b$, where "a" and "b" are two variable parameters, and b can be calculated from the slope of the plot of the log I vs log υ.[58] Normally, slope $b = 1/2$ exhibits the ideal diffusion-controlled faradaic process and that satisfies Cottrell's equation, $I = \upsilon^{1/2}$.[59]

However, slope $b = 1$ signifies electrochemical response for both faradic capacitance and double-layer capacitance, as the capacitive current is directly proportional to scan rates $I = \upsilon\,C_d A$, where specific capacitance is represented by "C_d" and the reactive surface area of the electrode material is represented by "A". Therefore, the process of electrochemical charge storage can be dominating at high sweep rates because of stronger linear dependency with the capacitive current; however, the diffusion process dominates at low scan rates. Furthermore, slope b, calculated by plotting the graph of log i vs log υ at various voltages(V), exhibits a value ~0.5 at peak potentials, which suggests the governance of the diffusion-controlled electrochemical storage process, while the slope value is ~1 at other potentials, signifying that the current is principally capacitive, as shown in Figure 9(a).

Insertion and extraction of ions at a lower scan rate and the available surface area significantly increase the storage capacity of charge. Therefore, it will be fascinating to examine the maximal charge that could be stored in Co-doped MnO$_2$ nanocomposites. The total charge stored in the synthesized electroactive material is computed by the method specified in the work by Trasatti et al.,[60] which includes the estimation of the total charge stored ($q*$total) using the intercept of the linear graph of $1/q*$ vs $\upsilon^{1/2}$, as shown in Figure 9(b).

This method is also useful to calculate the charge stored only at the external surface ($q*$external) of the synthesized electroactive material using the intercept of the linear graph of $q*$ vs $\upsilon^{-1/2}$, which is shown in Figure 9(c). Excitingly, the maximum charge that can be stored in the Co-doped MnO$_2$ nanocomposite is 1500 F/g, and on the external surface, the charge that can be stored is 274.64 F/g, which is comparable with the calculated specific capacitance for a potential window of 0.8 V. Furthermore, the charge stored on the internal surface ($q*$ internal) is the variance between the total charge ($q*$ total) and charge stored on the external surface ($q*$ external),
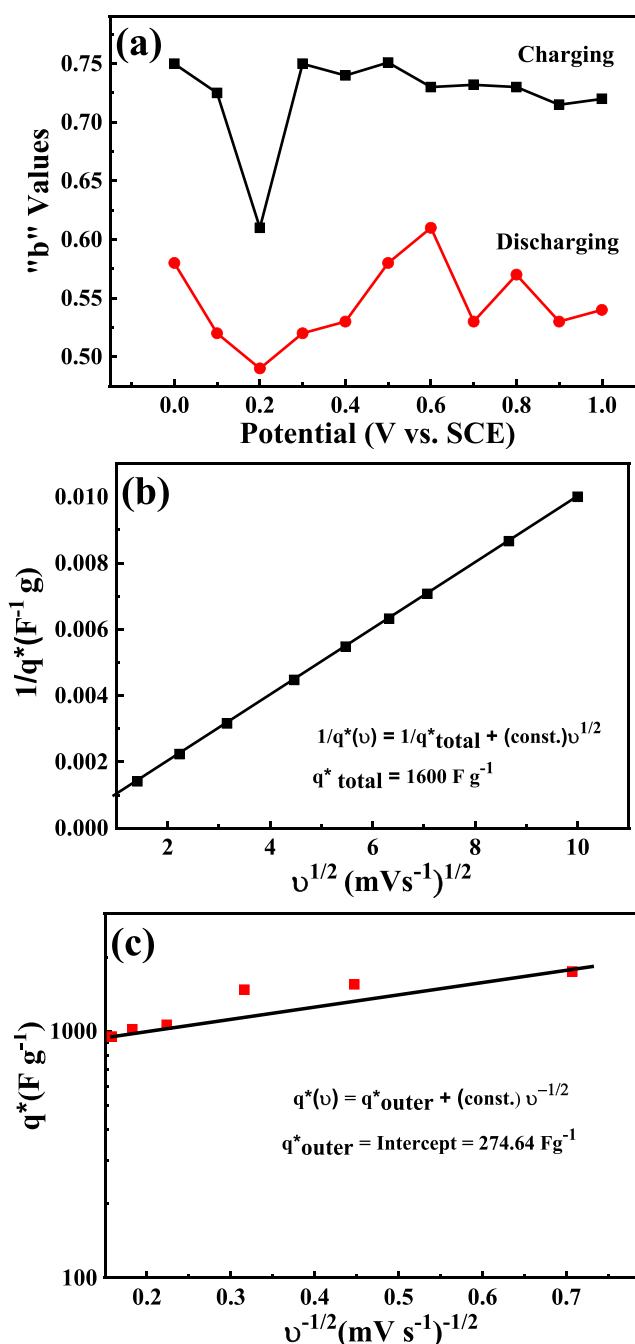
**Figure 9.** (a) Variation of slope "b" as a function of voltage(V) for cathodic and anodic sweeps of CV cycles and Trasatti plots. (b) Plot of $1/q*$ against $\upsilon^{1/2}$ to find the total charge ($q*$total) stored by the electrode material. (c) Plot of $q*$ against $\upsilon^{-1/2}$ to quantify the charge stored only on the outer surface of the electrode material ($q*$outer).

which is 1225.5 F/g. Because of the porous, fibrous, and spongy nature of the Co-doped MnO$_2$ nanocomposite, the active surface area for the inner and outer side increases. This is useful not only for faradaic but also for nonfaradaic processes at low and high scan rates, and because of the improvement in the active surface area, the charge storage capacity of the electrode material is also enhanced.

2.6. Galvanostatic Charge–Discharge. For the study of charge storage capacity and electrochemical stability of the synthesized electrode material, the galvanostatic charge–discharge measurement method can be used effectively. The

charging–discharging measurements of bare MnO_2 and Co-doped MnO_2 have been carried out in the voltage range 0 to 0.8 V at 0.5 A g^{-1} current density, which is exhibited in Figure 10(a). The specific capacitance value (C_{sp}) of the synthesized electrode material can be calculated from the discharging curve by using the following eq 3.

$$C_{sp} = \frac{I \times \Delta t}{m \times \Delta V} \tag{3}$$
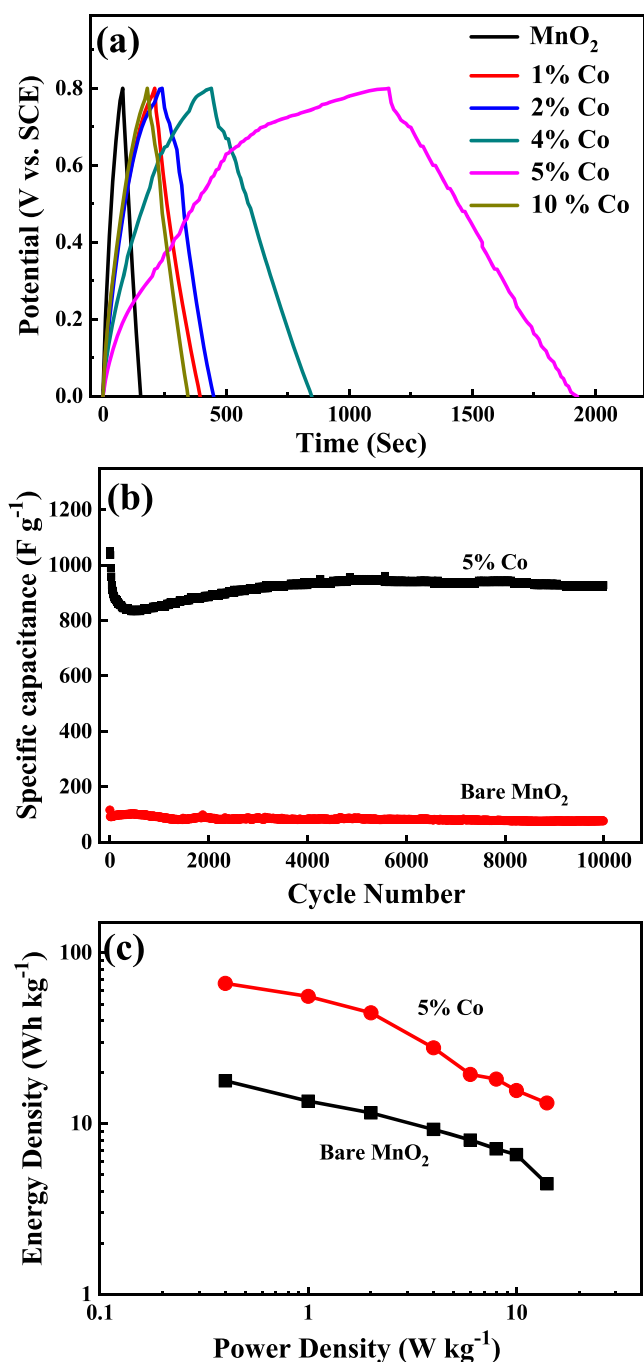
Figure 10. (a) Galvanostatic charge/discharge of S_0, S_1, S_2, S_3, S_4, and S_5 at 0.5 A g^{-1} current density. (b) Graph of the cycle number versus specific capacitance of S_0 and S_4 electrodes at a constant current density of 0.5 Ag^{-1}. (c) Ragone plot for S_0 and S_4 composite electrodes.

where I is the current (A), Δt is time (s), m (mg) is the loaded mass of active material of the electrode, and ΔV is a potential window(V). The charging–discharging curves are nearly symmetrical, which represents a highly reversible faradic reaction between the electrode and electrolyte, which are Co-doped MnO_2 and Na$^+$ ions, respectively. It is also responsible for the good capacitive behavior of the Co-doped MnO_2 nanocomposite. According to eq 3, the calculated specific capacitance at constant current density 0.5 A g^{-1} is 100 F g^{-1} for bare MnO_2 and 250, 281, 530, 1050, and 219 Fg^{-1} for S_1, S_2, S_3, S_4, and S_5, respectively. From these specific capacitance values, it is clear that all Co-doped MnO_2 nanocomposites contribute to the improvement of specific capacitance. It shows that because of the incorporation of Co into the MnO_2 nanostructure, electrical conductivity is improved, which helps to increase the specific capacitance and chemical diffusion coefficient of sodium in manganese dioxide.[61] Although the 10% Co-doped MnO_2 (S_5) nanocomposite exhibits a higher specific capacitance value than bare MnO_2, it is lower than that of the 5% Co-doped MnO_2 (S_4) nanocomposite. A fall in specific capacitance notifies that Co ions can enhance it up to the certain limit of Co concentration dopant.[62] It represents some limitations in pseudocapacitance reactions of synthesized nanocomposite electrodes with extra Co ions in the Na_2SO_4 electrolyte. Mainly, Co-based electrodes required a basic electrolyte such as NaOH or KOH with a small operational potential window for super-capacitor applications compared to the MnO_2-based nano-composite electrode. This may be one of the reasons for the low specific capacitance value at higher concentrations of cobalt in MnO_2-based electrodes. The observed specific capacitance values for the Co-doped MnO_2 nanocomposite in the current work are reasonably higher than the values reported for the cobalt-doped MnO_2 and Co_3O_4@MnO_2-based nanocomposites, which are compiled in Table 1.[13,63−69]

The relationship between specific capacitance and current density is given in Figure S2. It shows that current density is inversely proportional to the specific capacitance. The decrease in the specific capacitance value with the increasing current density is due to the little collaboration of active material with the electrolyte in the energy storage process, whereas for low current density, the accumulation process of the cation is slower and all the available active sites or pores get incorporated in the energy storage process.

This is why all active sites are wholly adsorbed and the materials are fully utilized, which resulted in increased specific capacitance at low current density.[33] The cyclic stability of undoped MnO_2 (S_0) and 5% Co-doped MnO_2 (S_4) electrodes is examined by galvanostatic charge–discharge measurements at a constant current density of 0.5 Ag^{-1} at about 10,000 cycles, as shown in Figure 10(b). Outstanding cycling stability, including retention of 92%, has been observed for 5% Co-doped MnO_2 (S_4) electrodes, with regard to their initial specific capacitance after 6000 cycles, which was higher than that of the MnO_2 electrode (80.7%). The capacitive perform-ance and cyclic stability of 5% Co-doped MnO_2 are better because Co ions enhance the electronic conduction of electrons within a metal oxide matrix.[70]

Figure S3 shows the plot of capacitance retention versus cycle number, which reveals the stability of charge stored as a function of the cycle number for bare MnO_2 and 5% Co-doped MnO_2 (S_4) at a current density of 0.5 Ag^{-1}. For application purposes, the supercapacitor electrode mostly relies on the

Table 1. Comparative Table for Specific Capacitance, Energy Density, and Power Density of the co-Doped MnO$_2$ Nanocomposite

electrode material	synthesis method	capacitance	cycle stability	ref.
Co$_3$O$_4$@MnO$_2$	hydrothermal	560 F g^{-1}at current density 0.2 Ag^{-1}	95% retention after 5000 cycles	13
Co$_3$O$_4$ nanowire@MnO$_2$	hydrothermal	480 F g^{-1} at current density 2.67 Ag^{-1}	2.7% loss after 5000 cycles	63
Co$_3$O$_4$@Pt@MnO$_2$	nanowire arrays on the Ti substrate coating	539 F g^{-1}at current density 1 Ag^{-1}	No loss after 5000 cycles	64
Co-doped MnO$_2$	pulse laser deposition	99 F g^{-1} at 5 mVs^{-1}	-	65
Co$_3$O$_4$@MnO$_2$ core−shell microspheres	hydrothermal	671 F g^{-1}at current density 1 A g^{-1}	5% loss after 2000 cycles	66
Co$_3$O$_4$@MnO$_2$/NGO	thermal reduction process	347 F g^{-1} at current density 0.5A g^{-1}	31% loss after 10,000 cycles	67
Co-doped MnO$_2$	light-assisted method	350 F g^{-1} at current density 0.1 A g^{-1}	10% loss after 1000 cycles	68
Co-doped MnO$_2$	pulsed electrodeposition	354 F g^{-1} at current density 0.5A g^{-1}	-	69
Co-doped MnO$_2$	hydrothermal	1050 F g^{-1}at current density 0.5 A g^{-1}	8% loss after 10,000 cycles	present work

cycle life of the electrode material, that is, the amount of specific capacity retained by the electrode material after constant galvanostatic charge−discharge cycling. It is important to note that the capacitance value of bare MnO$_2$ (S$_0$) gradually decreases during the galvanostatic charging−discharging. Capacitance loss is about 22% after the 1500th cycle. It may be due to the change in morphology of MnO$_2$ during cycling, which also induced lower ion/electron transformation, which affects the surface area and conductivity of the electrode.[24] The capacitance value of 5% Co-doped MnO$_2$ (S$_4$) electrode material decreased initially, followed by a slight increment. After 1500 cycles, there is about an 8% increment in the capacitance value, which may be due to a change in the electronic structure of MnO$_2$ cause by doping of Co ions.

Considering the applicability of supercapacitors, power density and energy density are two main parameters. Charging−discharging curves recorded at different current densities were used for calculating power density and energy density for bare MnO$_2$ (S$_0$) and 5% Co-doped MnO$_2$ (S$_4$) material. A variation of energy density versus power density was exhibited in the Ragone plot, as shown in Figure 10(c), for bare MnO$_2$ (S$_0$) and the 5% Co-doped MnO$_2$ (S$_4$) composite electrode. It is worthy to note that the 5% Co-doped MnO$_2$ (S$_4$) nanocomposite's stored energy density is 66.13 Wh kg^{-1} at a power density of 0.4 W kg^{-1}, which is much higher than that of bare MnO$_2$. Even at a high power density of 14 W kg^{-1}, the energy density of the 5% Co-doped (S$_4$) nanocomposite is 13.2 Wh kg^{-1}, which is still larger than that of the bare MnO$_2$ (S$_0$).

2.7. Electrochemical Impedance Spectroscopy. Electrochemical impedance spectroscopy (EIS) of the synthesized Co-doped MnO$_2$ nanocomposite was carried out to study the electrochemical behavior, charge transfer of undoped MnO$_2$ and Co-doped MnO$_2$ electrodes, and effect on internal resistance. EIS spectra are obtained after various charging/discharging cycles in the 100 kHz to 0.01 Hz frequency range along with 10 mV applied AC voltage at the open circuit potential. The Nyquist plot for bare MnO$_2$ and Co-doped MnO$_2$ electrodes presented in Figure 11(a) is composed of a spike and an incomplete semicircle at the low-frequency (inset of Figure 11a) and high-frequency areas, respectively, which exhibit good capacitive behavior and mediated resistance. At
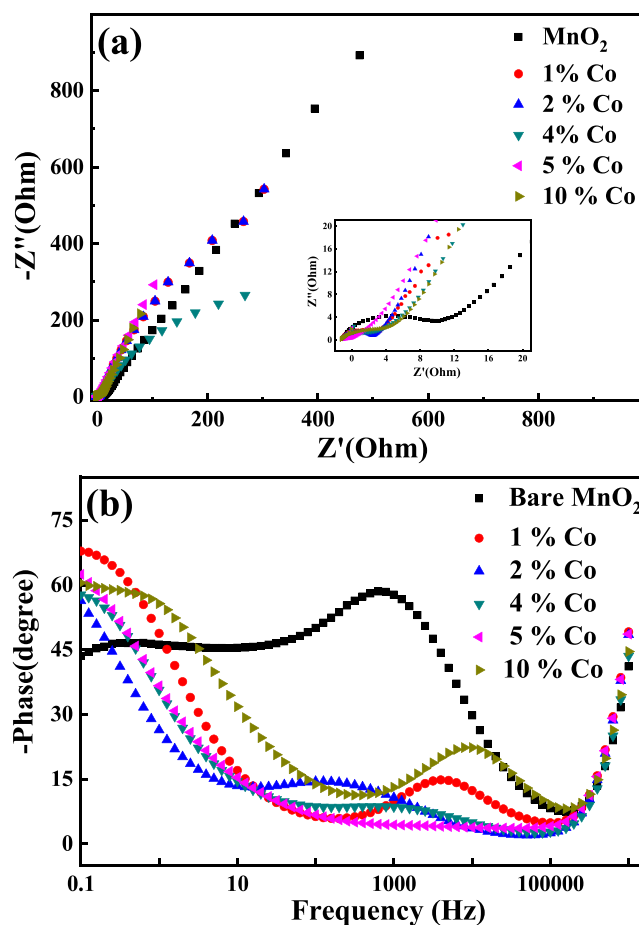

Figure 11. (a) Nyquist plots for bare MnO$_2$ and Co-doped MnO$_2$ electrodes and (b) Bode plots of bare MnO$_2$ and Co-doped MnO$_2$ electrodes.

the lower-frequency region, the spike shows an angle between 45 and 90° related to the real axis, which represents the process of diffusion control. As doping of Co ions increases, the overall value of electrode resistance was seen to decrease, which indicates the impact of Co ion doping on the electrode conductivity enhancement. Apart from this, Bode plots [Figure 11(b)] obtained from the variation in the phase angle degree

used various frequencies in the range of 10 mHz to 100 kHz for MnO_2 and Co-doped MnO_2 electrodes. With various concentrations of Co ions, for the MnO_2 electrodes, the phase angle degree remains near 90°, even at the high range of frequency, which indicates improved capacitive behavior of the synthesized electrodes.

2.8. Performance of Fabricated Solid-State Flexible Supercapacitors. Here, a prototype of a solid-state flexible supercapacitor device is fabricated and its electrochemical performance is analyzed by galvanostatic charging–discharging, which is shown in Figure 12. Figure 12(a) exhibits the
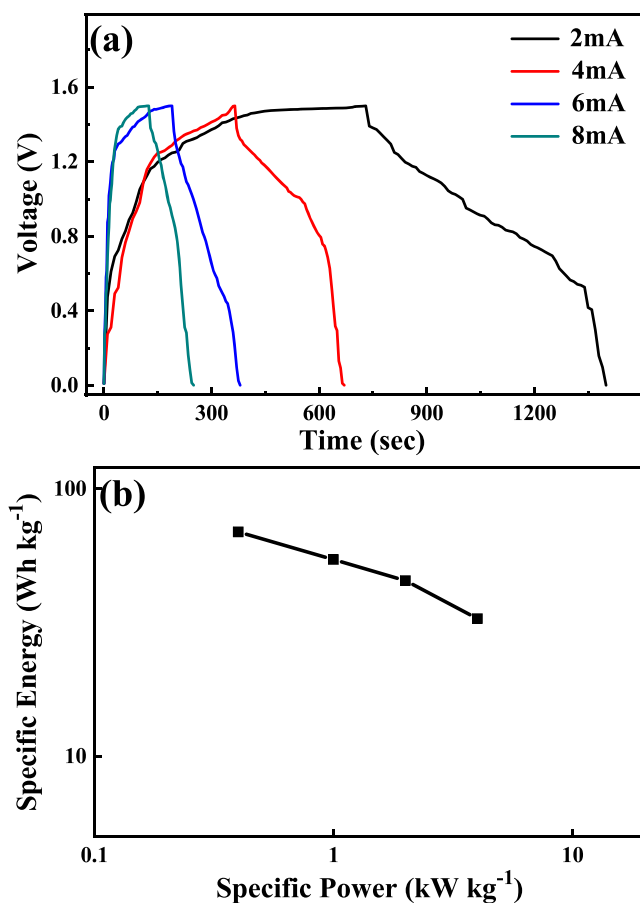

Figure 12. (a) Galvanostatic charge/discharge curves recorded at different applied current densities and (b) Ragone plot of the solid-state flexible supercapacitor device using Co-doped MnO_2 nanocomposites.

charging–discharging behavior of a solid-state flexible supercapacitor device composed of a Co-doped MnO_2 electrode between 0 and 1.5 V at a distinct current. The Co-doped MnO_2 electrode reveals fair charge–discharge time, suggesting high specific capacitance on the computational formula. The calculated values of specific capacitance of Co-doped MnO_2 nanocomposite-based symmetric devices are 933, 893, 760, and 660 F g^{-1} at an applied current of 2, 4, 6, and 8 mA, respectively. Figure 12(b) shows the Ragone plots of the Co-doped MnO_2 composite symmetric cell, indicating reliable charge storage performance with the maximum energy density of 69.3 Wh kg^{-1} at a power density of 0.4 kW kg^{-1}.

Here, successful fabrication of a simple solid-state flexible supercapacitor, which is based on the Co-doped MnO_2 electrode, is done by using the polyvinyl alcohol/Na_2SO_4 gel electrolyte, which is shown in [Figure 13(a,b)]. This device exhibits better electrochemical activity, flexibility, and power
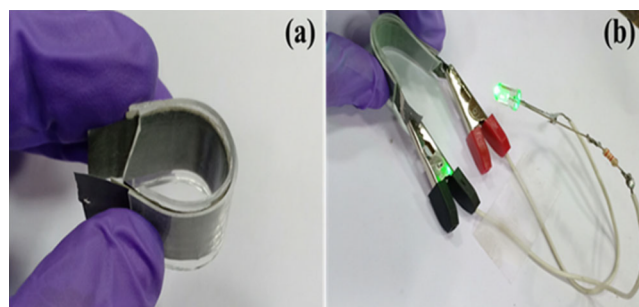
Figure 13. Photographs of (a) fabricated solid-state flexible supercapacitor device using the Co-doped MnO_2 nanocomposite. (b) Discharging of the fabricated device through LED (photograph courtesy—Sarika Jadhav).

and energy density than many other presently available supercapacitors. Ming et al. prepared Co_3O_4 @ MnO_2 core–shell arrays on Ni foam for asymmetric supercapacitors having an energy density of 17.7 Wh kg^{-1} and a maximum power density of 158 kW kg^{-1}.[13] Jianpeng et al. also prepared transitions of metal-doped MnO_2 having an energy density of 50 Wh kg^{-1} and a power density of 0.9 kWh kg^{-1}.[71] The current compositional and structural pattern indicated efficient and favorable way to improve the overall electrochemical performance of energy storage devices having an energy density of 69 Wh kg^{-1} and a power density of 0.4 kW kg^{-1}, which is better than the reported one, and it presented a pathway for their promising potential in energy management.

3. CONCLUSIONS

Here, a Co-doped MnO_2 nanocomposite was successfully synthesized using a simple single-step hydrothermal method for the fabrication of a flexible supercapacitor device. Because of the occurrence of different electrochemically active MnO_2 nanocrystalline phases, the MnO_2 electrode displayed high charge/discharge reversibility with a superb specific capacitance. By experimental evidence, it is proved that doping of definite amounts of Co ions in MnO_2 vigorously affects capacitive behavior and conductivity of the synthesized material. Among all added doping of Co concentrations, 5 mol % of Co-doped MnO_2 electrodes exhibited higher specific capacitance (1050 F g^{-1}) at a current density of 0.5 Ag^{-1} and excellent cycling stability (92%) over 10,000 cycles. The Co-doped MnO_2 composite solid-state flexible device demonstrates reliable charge storage performance with the maximum energy density of 69.3 Wh kg^{-1} at a power density of 0.4 kW kg^{-1}. By observing these remarkable results, we can conclude that incorporating a proper amount of Co ions in the MnO_2 nanocomposite with optimized hydrothermal condition offers an admirable commercial electrode material for energy storage application.

4. EXPERIMENTAL SECTION

4.1. Materials. Potassium permanganate ($KMnO_4$), sodium sulphate (Na_2SO_4), cobalt nitrate [Co $(NO_3)_2$], urea, ethanol (C_2H_6O), and so on were purchased from Sigma Aldrich, carbon black was purchased from Alfa Aesar, and N-Methyl-2 pyrrolidone (NMP) was obtained using high-performance liquid chromatography. All the solvents and

reagents are of analytical grade, and the solution was prepared in distilled water.

4.2. Co-Doped MnO₂ Nanomaterial Synthesis. $KMnO_4$, Co $(NO_3)_2$, and urea are precursors used for MnO_2 and Co-doped MnO_2 nanocomposite synthesis in the hydrothermal method. The process begins with dissolving $KMnO_4$ (0.2 M), urea, and essential mol percentage of Co $(NO_3)_2$ (1, 2, 4, 5, and 10 mol %) in 160 mL of distilled water, followed by intense stirring at room temperature till homogeneous solution was formed. After that, the homogeneous solution was poured into a 200 mL autoclave and retained a temperature of 140 °C in a hot air oven for 6 h. Subsequently, the autoclave was cooled normally to room temperature. After reaction impurities were removed by washing the product many times using ethanol and distilled water, and the product was collected after synthesis, dried at 80° C in the oven for 12 h, and utilized for additional characterization analysis. Finally, the powder samples obtained were denoted as S_0 for pristine manganese oxide, S_1 for 1% Co, S_2 for 2% Co, S_3 for 4% Co, S_4 for 5% Co, and S_5 for 10% Co-doped manganese oxide.

4.3. Characterization. A synthesized material nanocomposite was characterized for structural and elemental analysis and that can be related to its distinctive performance. An XRD study was done on a Bruker D8 Advance diffractometer with a CuKα radiation source. For the study, there was chemical bonding in the synthesized nanocomposite. Raman analysis was carried out, and the Renishaw InVia Raman microscope was used for spectra recording. The synthesized nanomaterials were analyzed using SEM (LEO-1550) for the morphological study. To study the electrochemical performance of the synthesized nanomaterial, a three-electrode system having platinum as a counter electrode, Ag/AgCl as a reference electrode, and synthesized material as a working electrode in an aqueous electrolyte solution of 1 M Na_2SO_4 was used. Evaluation of the capacitive performance of the synthesized nanomaterials was carried out by CV and galvanostatic charge−discharge test in the potential range of 0−0.9 V using an Autolab Potentiostat/ Galvanostat system PGSTAT128N (Metrohm).

4.4. Working Electrode Fabrication. For the fabrication of the working electrode, a paste of the synthesized nanocomposite was prepared by mixing the prepared manganese dioxide powder (80 wt %), PVDF binder (10 wt %), and carbon black (10 wt %) with NMP. By using the doctor blade method, the prepared homogeneous paste was uniformly coated on the conducting substrate electrode with a loading mass of 1−2 mg cm^{-2}. The prepared working electrodes were dried at 120 °C for 4 h in a vacuum oven to eliminate the NMP solvent.

■ ASSOCIATED CONTENT

ⓘ Supporting Information

The Supporting Information is available free of charge at https://pubs.acs.org/doi/10.1021/acsomega.0c06150.

EDS analysis data of the Co-doped MnO_2 sample; specific capacitance as a function of the scan rate; specific capacitance versus current density; and cycling performance of S_0 and S_4 electrodes (PDF).

■ AUTHOR INFORMATION

Corresponding Author

Suresh W. Gosavi − *Department of Physics, Savitribai Phule Pune University, Pune 411007, India;* ◉ orcid.org/0000-0001-7540-0664; Phone: +91-20-2562 2848; Email: swg@physics.unipune.ac.in; Fax: +91-20-2569 1684

Authors

Sarika M. Jadhav − *Department of Physics, Savitribai Phule Pune University, Pune 411007, India*

Ramchandra S. Kalubarme − *Nanocrystalline Materials, Centre for Materials for Electronic Technology, Pune 411008, India;* ◉ orcid.org/0000-0002-3327-5110

Norihiro Suzuki − *Photocatalysis International Research Center, Research Institute for Science & Technology, Tokyo University of Science, Noda 278-8510, Japan;* ◉ orcid.org/0000-0002-7154-3892

Chiaki Terashima − *Photocatalysis International Research Center, Research Institute for Science & Technology, Tokyo University of Science, Noda 278-8510, Japan;* ◉ orcid.org/0000-0002-8874-1481

Junyoung Mun − *Department of Energy & Chemical Engineering, Incheon National A University 119 Academy-ro Yeonsu-gu, Incheon 22012, S. Korea*

Bharat Bhanudas Kale − *Nanocrystalline Materials, Centre for Materials for Electronic Technology, Pune 411008, India;* ◉ orcid.org/0000-0002-3211-717X

Akira Fujishima − *Photocatalysis International Research Center, Research Institute for Science & Technology, Tokyo University of Science, Noda 278-8510, Japan*

Complete contact information is available at:
https://pubs.acs.org/10.1021/acsomega.0c06150

Notes

The authors declare no competing financial interest.

■ REFERENCES

(1) Wang, G.; Zhang, L.; Zhang, J. A review of electrode materials for electrochemical supercapacitors. *Chem. Soc. Rev.* **2012**, *41*, 797−828.

(2) Xiong, Z.; Hu, P.; Zhang, Y.; Cao, F.; Wang, D.; Sun, C.; Hu, Y.; Gu, H. All-Solid-State Supercapacitors Based on Flexible Co_3O_4 Nanoflowers/ rGO. *J. Electron. Mater.* **2018**, *47*, 5987−5992.

(3) Zhai, Y.; Dou, Y.; Zhao, D.; Fulvio, P. F.; Mayes, R. T.; Dai, S. Carbon Materials for Chemical Capacitive Energy Storage. *Adv. Mater.* **2011**, *23*, 4828−4850.

(4) Wang, K. X.; Wang, Y. G.; Wang, Y. R.; Hosono, E.; Zhou, H. S. Mesoporous Carbon Nanofibers for Supercapacitor Application. *J. Phys. Chem. C* **2009**, *113*, 1093−−1097.

(5) Xu, B.; Wu, F.; Chen, S.; Zhang, C.; Cao, G.; Yang, Y. Activated carbon fiber cloths as electrodes for high performance electric double-layer capacitors. *Electrochim.Acta* **2007**, *52*, 4595−4598.

(6) Pham, D. T.; Lee, T. H.; Luong, D. H.; Yao, F.; Ghosh, A.; Le, V. T.; Kim, T. H.; Li, B.; Chang, J.; Lee, Y. H. Carbon nanotube-bridged graphene 3D building blocks for ultrafast compact supercapacitors. *ACS Nano* **2015**, *9*, 2018–2027.

(7) Cao, X.; Shi, Y.; Shi, W.; Lu, G.; Huang, X.; Yan, Q.; Zhang, Q.; Zhang, H. Preparation of novel 3D graphene networks for supercapacitor applications. *Small* **2011**, *7*, 3163–3168.

(8) Hao, P.; Zhao, Z.; Tian, J.; Li, H.; Sang, Y.; Yu, G.; Cai, H.; Liu, H.; Wong, C. P.; Umar, A. Hierarchical porous carbon aerogel derived from bagasse for high-performance supercapacitor electrode. *Nanoscale* **2014**, *6*, 12120–12129.

(9) Yu, D.; Yao, J.; Qiu, L.; Wang, Y.; Zhang, X.; Feng, Y.; Wang, H. In situ growth of Co_3O_4 nanoparticles on α-MnO_2 nanotubes: a new hybrid for high-performance supercapacitors. *J. Mater. Chem.* **2014**, *2*, 8465–8471.

(10) Hu, C. C.; Chang, K. H.; Lin, M. C.; Wu, Y. T. Design and tailoring of nanotubular arrayed architecture of hydrous RuO_2 for next-generation supercapacitor. *Nano Letter* **2006**, *6*, 2690–2695.

(11) Qu, B.; Chen, Y.; Zhang, M.; Hu, L.; Lei, D.; Lu, B.; Li, Q.; Wang, Y.; Chen, L.; Wang, T. β-Cobalt sulfide nanoparticles decorated graphene composite electrodes for high capacity and power supercapacitors. *Nanoscale* **2012**, *4*, 7810–7816.

(12) Meng, C.; Liu, C.; Chen, L.; Hu, C.; Fan, S. Highly flexible and all-solid-state paperlike polymer supercapacitor. *Nano Lett.* **2010**, *10*, 4025–4031.

(13) Huang, M.; Zhang, Y.; Li, F.; Zhang, L.; Wen, Z.; Liu, Q. Facile synthesis of hierarchical $Co_3O_4@MnO_2$ core–shell arrays on Ni foam for asymmetric supercapacitors. *J. Power Sources* **2014**, *252*, 98–106.

(14) Huang, M.; Li, F.; Dong, F.; Zhang, Y. X.; Zhang, L. L. MnO_2-based nanostructures for high-performance supercapacitor. *J. Mater. Chem. A* **2015**, *3*, 21380–21423.

(15) Wang, W.; Guo, S.; Lee, I.; Ahmed, K.; Zhong, J.; Favors, Z.; Zaera, F.; Ozkan, M.; Ozkan, C. S. Hydrous Ruthenium Oxide Nanoparticles Anchored to Graphene and Carbon Nanotube Hybrid Foam for Supercapacitors. *Sci. Rep.* **2014**, *4*, 4452.

(16) Liao, Q.; Li, N.; Jin, S.; Yang, G.; Wang, C. All solid-state symmetric supercapacitor based on Co_3O_4 nanoparticles on vertically aligned graphene. *ACS Nano* **2015**, *9*, 5310–5317.

(17) Vijayakumar, S.; Nagamuthu, S.; Muralidharan, G. Supercapacitor studies on NiO nanoflakes synthesized through a microwave route. *ACS Appl. Mater. Interfaces* **2013**, *5*, 2188–2196.

(18) Wang, Q.; Zou, Y.; Xiang, C.; Chu, H.; Zhang, H.; Xu, F.; Sun, L.; Tang, C. High-performance supercapacitor based on V_2O_5/carbon nanotubes-super activated carbon ternary composite. *Ceram. Int.* **2016**, *42*, 12129–12135.

(19) Hu, Y.; Guan, C.; Ke, Q.; Yow, Z. F.; Cheng, C.; Wang, J. Hybrid Fe_2O_3 nanoparticles clusters/rGO paper as an effective negative electrode for flexible supercapacitor. *Chem.Mater* **2016**, *28*, 7296–7303.

(20) Dubal, D. P.; Gund, G. S.; Lokhande, C. D.; Holze, R. CuO cauliflowers for supercapacitor application: Novel potentiodynamic deposition. *Mater. Res. Bull.* **2013**, *48*, 923–928.

(21) Li, L.; Qin, Z. Y.; Wang, L. F.; Liu, H. J.; Zhu, M. F. Anchoring alpha-manganese oxide nanocrystallites on multi-walled carbon nanotubes as electrode materials for supercapacitor. *J. Nanopart Res.* **2010**, *12*, 2349––2353.

(22) Zhu, G.; He, Z.; Chen, J.; Zhao, J.; Feng, X.; Ma, Y.; Fan, Q.; Wanga, L.; Huang, W. Highly conductive three-dimensional MnO_2–carbon nanotube–graphene–Ni hybrid foam as a binder-free supercapacitor electrode. *Nanoscale* **2014**, *6*, 1079–1085.

(23) Wei, W.; Cui, X.; Chen, W.; Ivey, D. G. Manganese oxide-based materials as electrochemical supercapacitor electrodes. *Chem. Soc. Rev.* **2011**, *40*, 1697–1721.

(24) Tanggarnjanavalukul, C.; Phattharasupakun, N.; Kongpatpanich, K.; Sawangphruk, M. Charge storage performances and mechanisms of MnO_2 nanospheres, nanorods, nanotubes, and nanosheets. *Nanoscale* **2017**, *9*, 13630–13639.

(25) Xiong, G.; Hembrama, K. P. S. S.; Reifenberger, R. G.; Fisher, T. S. MnO_2-coated graphitic petals for supercapacitor electrodes. *J. Power Source* **2013**, *227*, 254–259.

(26) Zhang, Y. X.; Huang, M.; Li, F.; Wang, X. L.; Wen, Z. Q. One-pot synthesis of hierarchical MnO_2-modified diatomites for electrochemical capacitor electrodes. *J. Power Sources* **2014**, *246*, 449–456.

(27) Xu, L.; Jia, M.; Li, Y.; Jin, X.; Zhang, F. High-performance MnO_2-deposited graphene/activated carbon film electrodes for flexible solid-state supercapacitor. *Sci. Rep.* **2017**, *7*, 12857–12867.

(28) Meng, X.; Lu, L.; Sun, C. Green Synthesis of Three-Dimensional MnO_2/Graphene Hydrogel Composites as a High-Performance Electrode Material for Supercapacitors. *ACS Appl. Mater. Interfaces* **2018**, *19*, 16474–16481.

(29) Venkat, S.; Weidner, J. W. Capacitance studies of cobalt oxide films formed via electrochemical precipitation. *J. Power Sources* **2002**, *108*, 15–20.

(30) Chang, J. K.; Lee, M. T.; Huang, C. H.; Tsai, W. T. Physicochemical properties, and electrochemical behavior of binary manganese–cobalt oxide electrodes for supercapacitor applications. *Mater. Chem. Phys.* **2008**, *108*, 124–131.

(31) Wang, Y.; Guan, H.; Du, S.; Wang, Y. A facile hydrothermal synthesis of MnO_2 nanorod– reduced graphene oxide nanocomposites possessing excellent microwave absorption properties. *RSC Adv.* **2015**, *5*, 88979–88988.

(32) Zhu, C.; Yang, L.; Seo, J. K.; Zhang, X.; Wang, S.; Shin, J. W.; Chao, D.; Zhang, H.; Meng, Y. S.; Fan, H. J. Self-branched α-MnO_2/δ-MnO_2 heterojunction nanowires with enhanced pseudocapacitance. *Mater. Horiz.* **2017**, *4*, 415–422.

(33) Zhang, X.; Yu, P.; Zhang, H.; Zhang, D.; Sun, X.; Ma, Y. Rapid hydrothermal synthesis of hierarchical nanostructures assembled from ultrathin birnessite-type MnO_2 nanosheets for supercapacitor applications. *Electrochim. Acta* **2013**, *89*, 523–529.

(34) Julien, C. M.; Mauger, A. Nanostructured MnO_2 as Electrode Materials for Energy Storage. *Nanomaterials* **2017**, *7*, 396–437.

(35) Yu, L. L.; Zhuac, J. J.; Zhao, J. T. Beta-manganese dioxide nanoflowers self-assembled by ultrathin nanoplates with enhanced supercapacitive performance. *J. Mater.Chem.A* **2014**, *2*, 9353–9360.

(36) Li, W. N.; Yuan, J.; Shen, X. F.; Gomez-Mower, S.; Xu, L. P.; Sithambaram, S.; Aindow, M.; Suib, S. L. Hydrothermal Synthesis of Structure- and Shape-Controlled Manganese Oxide Octahedral Molecular Sieve Nanomaterials. *Adv. Fun. Mater* **2006**, *16*, 1247–1253.

(37) Xun, W.; Yadong, L. Synthesis and Formation Mechanism of Manganese dioxide Nanowires/Nanorods. *Chem. — Eur. J.* **2003**, *9*, 300–306.

(38) Chen, L.; Ding, J.; Jia, J.; Ran, R.; Zhang, C.; Song, X. Cobalt-Doped MnO_2 Nanofibers for Enhanced Propane Oxidation. *ACS Appl. Nano Mater.* **2019**, *2*, 4417–4426.

(39) Kuang, P. Y.; Liang, M. H.; Kong, W. Y.; Liu, Z. Q.; Guo, Y. P.; Wang, H. J.; Li, N.; Su, Y. Z.; Chen, S. Anion-assisted one-pot synthesis of 1D magnetic α and β-MnO_2 nanostructures for recyclable water treatment application. *New J. Chem.* **2015**, *39*, 2497–2505.

(40) Wang, G.; Shao, G.; Du, J.; Zhang, Y.; Ma, Z. Effect of doping cobalt on the micro-morphology and electrochemical properties of birnessite $MnO2$. *Mater. Chem. Phys.* **2013**, *138*, 108–113.

(41) Randi, N. M.; Fen, Y. W.; Omar, N. A.; Azis, R. S.; Zaid, M. H. Effects of cobalt doping on structural, morphological, and optical properties of Zn_2SiO_4 nanophosphors prepared by sol-gel method. *Results in Phys.* **2017**, *7*, 3820–3825.

(42) Zahid, M. A.; Barman, S. C.; Toyabur, R. M.; Sharifuzzaman, M.; Xuan, X.; Nah, J.; Park, J. Y. Ex Situ Hybridized Hexagonal Cobalt Oxide Nanosheets and RGO@MWCNT Based Nanocomposite for Ultra-Selective Electrochemical Detection of Ascorbic Acid, Dopamine, and Uric Acid. *J. Electrochem. Soc.* **2019**, *166*, B304–B311.

(43) Shrestha, K. R.; Kandula, S.; Rajeshkhanna, G.; Srivastava, M.; Kim, N. H.; Lee, J. H. An advanced sandwich-type architecture of $MnCo_2O_4@N$–$C@MnO_2$ as an efficient electrode material for a high-energy-density hybrid asymmetric solid-state supercapacitor. *J. Mater. Chem. A* **2018**, *6*, 24509–24522.

(44) Shrestha, K. R.; Kandula, S.; Kim, N. H.; Lee, J. H. A spinel $MnCo_2O_4$/NG 2D/2D hybrid nanoarchitectures as advanced electrode material for high-performance hybrid supercapacitors. *J. Alloys Compd.* **2019**, *771*, 810−820.

(45) Bin, D.; Guo, Z.; Tamirat, A. G.; Ma, Y.; Wang, Y.; Xia, Y. Crab-shell induced synthesis of ordered macroporous carbon nanofiber arrays coupled with $MnCo_2O_4$ nanoparticles as bifunctional oxygen catalysts for rechargeable Zn−air batteries. *Nanoscale* **2017**, *9*, 11148−11157.

(46) Huang, M.; Zhao, X. L.; Li, F.; Li, W.; Zhang, B.; Zhang, Y. X. Synthesis of Co_3O_4/SnO_2@MnO_2 core-shell nanostructures for high-performance supercapacitors. *J. Mater. Chem. A* **2015**, *3*, 12852−12857.

(47) Condon, J. B.; *Surface Area and Porosity Determinations by Physisorption*. Elsevier Science, First edition; 2016.

(48) Yan, H.; Bai, J.; Liao, M.; He, Y.; Liu, Q.; Liu, J.; Zhang, H.; Li, Z.; Wang, J. One-Step Synthesis of Co_3O_4/Graphene Aerogels and Their All-Solid-State Asymmetric Supercapacitor. *Eur. J. Inorg. Chem.* **2017**, 1143−1152.

(49) Cao, J.; Safdar, M.; Wang, Z.; He, J. High-performance flexible supercapacitor electrodes based on Te nanowire arrays. *J. Mater. Chem. A* **2013**, *1*, 10024−10029.

(50) Singh, G. M.; Micha, R.; Khatibzadeh, S.; Mozaffarian, D. Global, Regional, and National Consumption of Sugar-Sweetened Beverages, Fruit Juices, and Milk: A Systematic Assessment of Beverage Intake in 187 Countrie. *PLoS One* **2015**, 2−16.

(51) Chen, W.; Fan, Z.; Gu, L.; Bao, X.; Wang, C. Enhanced capacitance of manganese oxide via confinement inside carbon nanotubes. *Chem. Commun.* **2010**, *46*, 3905−3907.

(52) Brousse, T.; Toupin, M.; Dugas, R.; Athouël, L.; Crosnier, O.; Bálanger, D. Crystalline MnO_2 as Possible Alternatives to Amorphous Compounds in Electrochemical Supercapacitors. *J. of Electrochem. Soc.* **2006**, *153*, A171−A180.

(53) Ghodbane, O.; Pascal, J. L.; Favier, F. Microstructural Effects on Charge-Storage Properties in MnO_2-Based Electrochemical Supercapacitors. *ACS Appl. Mat. Interfaces* **2009**, *1*, 1130−1139.

(54) Inamdar, A. I.; Kim, Y. S.; Sohn, J. S.; Im, H.; Kim, H.; Kim, D. Y. Supercapacitive Characteristics of Electrodeposited Polyaniline Thin Films Grown on Indium-doped Tin-oxide Substrates. *J. Korean Phys. Soc.* **2011**, *59*, 145−149.

(55) Tang, X. H.; Li, H. J.; Liu, Z. H.; Yang, Z. P.; Wang, Z. L. Preparation and capacitive property of manganese oxide nanobelt bundles with birnessite-type structure. *J. Power Sources* **2011**, *196*, 855−859.

(56) Rusi, M. S. R. Controllable synthesis of flowerlike α-MnO_2 as electrode for pseudocapacitors application. *Solid State Ionics* **2014**, *262*, 220−225.

(57) Sathiya, M.; Prakash, A. S.; Ramesha, K.; Tarascon, S. J. M. V_2O_5-Anchored Carbon Nanotubes for Enhanced Electrochemical Energy Storage. *J.Am.Chem.Soc.* **2011**, *133*, 16291−16299.

(58) Lindstrom, H.; Sodergren, S.; Solbrand, A.; Rensmo, H.; Hjelm, J.; Hagfeldt, A.; Lindquist, S. E. Li^+ Ion Insertion in TiO_2 (Anatase). 2. Voltammetry on Nanoporous Films. *J. Phys. Chem. B* **1997**, *101*, 7717−7722.

(59) Wang, J.; Polleux, J.; Lim, J.; Dunn, B. Pseudocapacitive Contributions to Electrochemical Energy Storage in TiO_2 (Anatase) Nanoparticles. *J. Phys. Chem. C* **2007**, *111*, 14925−14931.

(60) Ardizzone, S.; Fregonara, G.; Trasatti, S. "Inner" and "Outer" Active Surface of RuO_2 Electrodes. *Electrochim. Acta* **1990**, *35*, 263−267.

(61) Sharma, P. K.; Moore, G. J.; Zhang, F.; Zavalij, P.; Whittingham, M. S. Electrical Properties of the Layered Manganese Dioxides M $xMn_1 _ yCoy$ O $_2$, M = Na, K Electrochem. *Solid-State Lett.* **1999**, *2*, 494−496.

(62) Nakayama, M.; Suzuki, K.; Okamura, K.; Athoue, L.; Crosnier, O.; Brousse, T. Doping of Cobalt into Multilayered Manganese Oxide for Improved Pseudocapacitive Properties. *J. Electrochem. Soc.* **2010**, *157*, 1067−1072.

(63) Liu, J.; Jiang, J.; Cheng, C.; Li, H.; Zhang, J.; Gong, H.; Fan, H. J. Co_3O_4 Nanowire@MnO_2 Ultrathin Nanosheet Core/Shell Arrays: A New Class of High-Performance Pseudocapacitive Materials. *Adv. Mater.* **2011**, *23*, 2076−2081.

(64) Xia, H.; Zhu, D.; Luo, Z.; Yu, Y.; Shi, X.; Yuan, G.; Xie, J. Hierarchically Structured Co_3O_4@Pt@ MnO_2 Nanowire Arrays for High-Performance Supercapacitors. *Sci. Rep.* **2013**, *3*, 2978−2986.

(65) Yang, D. Pulsed laser deposition of cobalt-doped manganese oxide thin films for supercapacitor applications. *J. Power Sources* **2012**, *198*, 416−422.

(66) Che, H.; Lv, Y.; Liu, A.; Mu, J.; Zhang, X.; Bai, Y. Facile synthesis of three dimensional flower-like Co_3O_4@MnO_2 core-shell microspheres as high-performance electrode materials for supercapacitors. *CeramicsInter.* **2017**, 148.

(67) Ramesh, S.; Karuppasamy, K.; Kim, H. S.; Kim, H. S.; Kim, J. H. Hierarchical Flowerlike 3D nanostructure of Co_3O_4@MnO_2/ N-doped Graphene oxide (NGO) hybrid composite for a high-performance supercapacitor. *Sci. Rep.* **2018**, *8*, 16543−16554.

(68) Tang, C. L.; Wei, X.; Jiang, Y. M.; Wu, X. Y.; Han, L. N. K.; Wang, X.; Chen, J. S. Cobalt-Doped MnO2 Hierarchical Yolk−Shell Spheres with Improved Supercapacitive Performance. *J. Phys. Chem. C* **2015**, *119*, 8465−8471.

(69) Wang, G.; Wang, W.; Zhao, Y.; Shao, G.; Liu, T.; Ma, Z. Pulsed electrodeposition of mesoporous cobalt-doped manganese dioxide as supercapacitor electrode material. *Ionics* **2014**, *20*, 243−249.

(70) Kim, B. C.; Wallace, G. G.; Yoon, Y. I.; Ko, J. M.; Too, C. O. Capacitive properties of RuO_2 and Ru−Co mixed oxide deposited on single-walled carbon nanotubes for high- performance supercapacitors. *Synt. Met.* **2009**, *159*, 1389−1392.

(71) Li, J.; Ren, Y.; Wang, S.; Ren, Z.; Yu, J. Transition metal-doped MnO_2 nanosheet grown on internal surface of macroporous carbon for supercapacitors and oxygen reduction reaction electrocatalysts. *Appl.Mater. Today* **2016**, *3*, 63−72.